Nuclear Science and Techniques (2023) 34:134
https://doi.org/10.1007/s41365-023-01290-4

Study on the gamma rays and neutrons energy response optimization of a scintillating fiber detector for EAST with Geant4

Wei-Kun Chen[1,2] · Li-Qun Hu[1] · Guo-Qiang Zhong[1,3] · Rui-Jie Zhou[1] · Bing Hong[3] · Qiang Li[1,2] · Li Yang[1,2]

Received: 28 February 2023 / Revised: 26 May 2023 / Accepted: 30 May 2023 / Published online: 20 September 2023

Abstract

A new scintillating fiber detector inside magnetic shielding tube was designed and assembled for use in the next round of fusion experiments in the experimental advanced superconducting tokamak to provide D–T neutron yield with time resolution. In this study, Geant4 simulations were used to obtain the pulse height spectra for ideal signals produced when detecting neutrons and gamma rays of multiple energies. One of the main sources of interference was found to be low-energy neutrons below 10^{-5} MeV, which can generate numerous secondary particles in the detector components, such as the magnetic shielding tube, leading to high-amplitude output signals. To address this issue, a compact thermal neutron shield containing a 1-mm Cd layer outside the magnetic shielding tube and a 5-mm inner Pb layer was specifically designed. Adverse effects on the measurement of fast neutrons and the shielding effect on gamma rays were considered. This can suppress the height of the signals caused by thermal neutrons to a level below the height corresponding to neutrons above 4 MeV because the yield of the latter is used for detector calibration. In addition, the detector has relatively flat sensitivity curves in the fast neutron region, with the intrinsic detection efficiencies (IDEs) of approximately 40%. For gamma rays with energies that are not too high (<8 MeV), the IDEs of the detector are only approximately 20%, whereas for gamma rays below 1 MeV, the response curve cuts off earlier in the low-energy region, which is beneficial for avoiding counting saturation and signal accumulation.

Keywords Sci-Fi detector · D–T fusion neutron · Thermal neutron shield · Energy response · Geant4

1 Introduction

Currently, a commonly used approach for assessing the confinement of α particles in D–D fusion experiments is the indirect study of the behavior of tritons produced by D–D fusion in deuterium plasma [1]. In this approach, the measurement of 14-MeV neutrons generated by the t(d, n)α fusion reaction is one of the main study methods, and it has been used in tokamak experiments such as DIII-D [2, 3], FT [4, 5], TFTR[6–8], JET [9–11], ASDEX [12], KSTAR [13–15], LHD [16–19], and JT-60U [20–22]. Among the existing D–T neutron measurement systems on EAST [23], the neutron activation system (NAS) [24], which has been established in recent years, currently uses silicon samples as activation materials and the ^{28}Si (n, p)^{28}Al reaction with a threshold of 4 MeV to measure the neutron yield of D–T fusion. Although the NAS does not have time resolution, the absolute yield provided is usually used for calibrating other neutron diagnostic systems. By comparison, the existing 4H-SiC detector [25] can provide real-time monitoring of D–T neutrons in

This work was supported by the University Synergy Innovation Program of Anhui Province (No. GXXT-2022-001), the Institute of Energy, Hefei Comprehensive National Science Center (Anhui Energy Laboratory) under Grant No. 21KZS205 and 21KZL401, and the Comprehensive Research Facility for Fusion Technology Program of China (No. 2018-000052-73-01-001228).

✉ Guo-Qiang Zhong
gqzhong@ipp.ac.cn

1 Institute of Plasma Physics, Hefei Institutes of Physical Science, Chinese Academy of Sciences, Hefei 230031, China

2 University of Science and Technology of China, Hefei 230026, China

3 Institute of Energy, Hefei Comprehensive National Science Center (Anhui Energy Laboratory), Hefei 230031, China

theory; however, it may not perform at its full capacity in cases of low D–T neutron yield in deuterium plasma, owing to its small size and low detection efficiency. The newly developed plastic scintillating fiber (Sci-Fi) detector [26] has a larger sensitive size, and its fast response leads to good time resolution; therefore, it is more suitable for the current situation of experimental advanced superconducting tokamak (EAST) and will be used in the next round of experiments. Because of its special structure, the Sci-Fi detector can effectively suppress the pulse signals caused by gamma rays to achieve particle resolution between neutrons and gamma rays by setting a threshold. Because the recoil proton energy is proportional to the energy of the incident neutron, neutrons with different energies can also be identified by setting different thresholds. For the above reasons, the influence of the surrounding radiation on the Sci-Fi detector is generally not specifically investigated because the heights of the pulse signals generated by X/γ-rays and thermal neutrons in the environment are considered negligible compared to those of the 14-MeV D–T fusion neutrons.

To reduce the interference of electromagnetic pulses on the photomultiplier tube (PMT), the Sci-Fi detector to be used on EAST will be securely housed within a magnetic shielding tube made of permalloy. As this tube also interacts with incident particles in an environment with high neutron and gamma-ray fluxes, the detection effect of the complete detector model (including the magnetic shielding tube) on neutrons and gamma rays of different energies should be tested. Referring to the neutron capture cross sections of Ni, Fe, and other elements in permalloys [27], it is foreseeable that thermal neutrons of low energy but extremely high flux will become the main interfering particles. This is because the proximity of the magnetic shielding tube to the Sci-Fi detector and the secondary particles produced by the neutron capture reaction may have a significant influence on the detector. The design of thermal neutron shields for Sci-Fi detectors operating on TFTR and the JT-60U has already been performed by their team. In this study, the Monte Carlo method [28] was applied to simulate the output pulse height spectra of the detector to be used on EAST and to guide the design of the radiation shield. In addition, the energy response characteristics of the new model are discussed.

2 Sci-Fi detector model

The Sci-Fi detector intended for use on EAST was designed to suit a specific radiation environment, and its structure is presented in Fig. 1. The Sci-Fis are embedded and fixed in the substrate of the detector head with a polished aluminum foil placed at the front end to serve as a light reflection layer. The plastic Sci-Fi model used in this detector is based on the Kuraray SCSF-78 M [29] and has a 1 mm diameter with

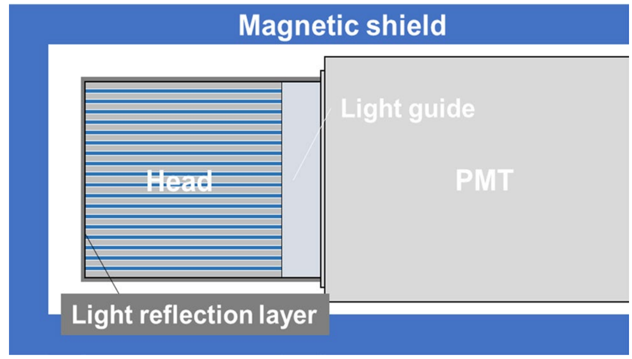

Fig. 1 Structure of the Sci-Fi detector (with the magnetic shielding tube)

a double-cladding structure to reduce scintillation photon leakage and increase light transmission efficiency. To avoid the scintillation photons emitted from the Sci-Fis focusing on a small range on the photocathode, a light guide is employed to connect the ends of all Sci-Fis to the PMT and disperse the photon output by each fiber to a larger area. The insulated light guide can also avoid direct contact between the substrate of the metal material and the end face of the PMT, which may cause the latter to fail to apply a high voltage normally. To ensure a uniform minimum spacing between adjacent fibers, the Sci-Fis were multistacked in a trefoil shape. The incident neutrons entering the core layer of Sci-Fis deposit energy by ejecting recoil protons through elastic scattering with hydrogen atoms. Therefore, the maximum number of produced scintillation photons and the maximum height of the pulse signals finally output by the PMT are positively correlated with their energies. By contrast, incident gamma photons undergo Compton scattering and a low-probability electron-pair effect in the fiber, generating numerous electrons and a few positrons. The substrate between the Sci-Fis can reduce the escape of these secondary particles from the first fiber, where they are produced, to adjacent fibers. Compared to the secondary electron, the recoil proton has a greater energy loss per unit path length ($\mathrm{d}E/\mathrm{d}x$) and can easily deposit energy in the first fiber, resulting in different energy deposition efficiencies between the neutrons and gamma rays in Sci-Fis. This is why the Sci-Fi detector has good n/γ resolution. Therefore, in an ideal case, the resolution of n/γ particles or neutrons of different energies can be achieved by setting a reasonable threshold for the signal amplitude.

In our previous study, we used a 14-MeV neutron source corresponding to D–T fusion neutrons and a 15-MeV gamma-ray source to optimize the material and structure of the Sci-Fi detector, so that its relative n/γ resolution and intrinsic detection efficiency (IDE) could meet the requirements of D–T neutron detection on EAST. The results demonstrated that a 5-cm probe head made of pure aluminum, in which 463 Sci-Fis were embedded with the same length of 5 cm and a minimum distance of 2 mm between their centers, was the optimal design scheme [26]. In this study, we further tested the detector made based on the above conclusions to determine its response characteristics to neutrons and gamma rays of multiple energies. It should be emphasized that the magnetic shielding tube made of permalloy is considered a part of the Sci-Fi detector system and was included in all models in both previous study and the current study.

3 Simulation and evaluation criteria

Geant4 [30] is a toolkit that uses the Monte Carlo method to simulate the passage of particles through matter. The version used in this study was 10.5.1, and the physical list and other optical settings were the same as those in [26]. The effective attenuation length of the fiber core for the scintillation photons was determined based on [31]. During the EAST experiment, gamma rays around the device were typically concentrated in the energy range below 3 MeV [32]. However, the use of neutral beam injection (NBI) cannot be ignored, which is one of the major auxiliary heating methods on EAST and plays an important role in plasma confinement [33–36]. Considering the very few gamma rays with energies above 10 MeV during the discharges when the NBI is in high-power operation, the maximum energy of the gamma-ray source used in the simulations was set to 15 MeV. For neutrons, we used 14 MeV as the highest energy to simulate those produced by the D–T fusion reaction and 2.45 MeV for the D–D fusion neutrons. In the energy range above 1 MeV, the particle source energy of the same group of simulation experiments varied at 1-MeV intervals and decreased exponentially below 1 MeV. The number of emitted source particles was set as 2×10^8 to ensure reliable calculation results.

To simplify the model and improve its computational efficiency, the Sci-Fi detector models for the Geant4 simulation excluded the PMT part. As the signal amplification process in the PMT is essentially linear, we used the number of scintillation photons emitted from the rear end of the light guide during an event (i.e., the entire simulation process caused by one source particle) to characterize the height of the ideal final pulse signal. Therefore, the threshold of the signal amplitude set for discriminating incident neutrons and gamma rays of different energies was converted into the threshold of the maximum number of photons output by the light guide during an event. It must be noted that the pulse signal, in reality, has a time length; thus, pulse integral spectra are often used as well as the pulse height spectra. In addition, as the use of absolute counts results in errors between different groups of simulations, normalized relative counts were used in this study.

The baseline was the maximum number of photons produced by a 4-MeV neutrons output in an event, corresponding to the maximum height of all signals they can produce. This choice was made to facilitate comparison and calibration using NAS because the energy threshold of the ^{28}Si (n, p) ^{28}Al reaction occurring in the silicon samples was 4 MeV. The normalized ratio was abbreviated as $H_{\max}$ ratio and used as a parameter to evaluate the detector's resolution for n/γ particles or neutrons of different energies. The formula is as follows:

$$H_{\max}\ \text{ratio} = \frac{H_{\max,i}}{H_{\max,n(4\,\text{MeV})}} = \frac{N_{\max,i}}{N_{\max,n(4\,\text{MeV})}},$$

where $H_{\max,n(4\,\text{MeV})}$ denotes the maximum height of the pulse signals when the source particles are 4-MeV neutrons, and $N_{\max,n(4\,\text{MeV})}$ denotes the maximum count of scintillation photons output from the rear end of the light guide in an event when the source particles were the same; in contrast, $H_{\max,i}$ and $N_{\max,i}$ correspond to the case when particle sources of different types or energies are used.

In addition, the detection efficiency (DE) and intrinsic detection efficiency (IDE) were tested to characterize the sensitivity of the detector to neutrons and gamma rays of different energies. The energy response curve of the detector is presented in this paper. The DE was calculated using the following formula:

$$\text{DE} = \frac{N_{\text{eff}}}{N_{\text{in,total}}} = \frac{N_{\text{out}}}{N_{\text{in,front}}}.$$

The IDE was characterized by the following formula:

$$\text{IDE} = \frac{N_{\text{eff}}}{N_{\text{in,eff}}} = \frac{N_{\text{out}}}{N_{\text{in.fib}} + N_{\text{in.sub}}},$$

where N_{eff} denotes the number of events that generate the output signal; $N_{\text{in,total}}$, which is also called $N_{\text{in,front}}$, denotes the number of events with source particles entering the complete detector model from the front; N_{out} denotes the number of events with photons exiting from the end of the light guide; and $N_{\text{in,eff}}$ denotes the number of events in which the incoming source particles enter the probe head, which can be divided into two parts, $N_{\text{in.fib}}$ and $N_{\text{in.sub}}$. The former denotes the number of events in which particles enter the Sci-Fis, whereas the latter denotes the number of events in which the particles only enter the probe head substrate and do not enter the fibers.

4 Simulation results

The reliability of the detector model was confirmed by comparing the Geant4 simulation results with the experimental data, as depicted in Fig. 2. The simulation of ^{252}Cf

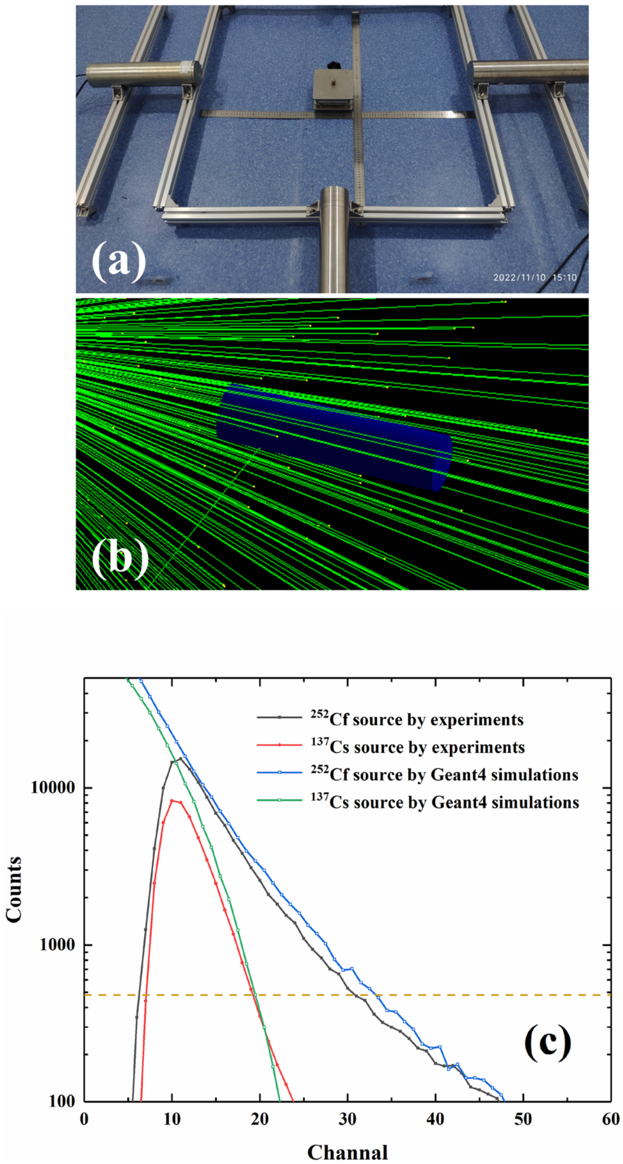

Fig. 2 (Color online) **a** Experiment and **b** simulation of the Sci-Fi detector. **c** Comparison of the Geant4 simulation results of the detector model and experimental results. The yellow dotted baseline represents the case where the count reached 10 in the simulation results

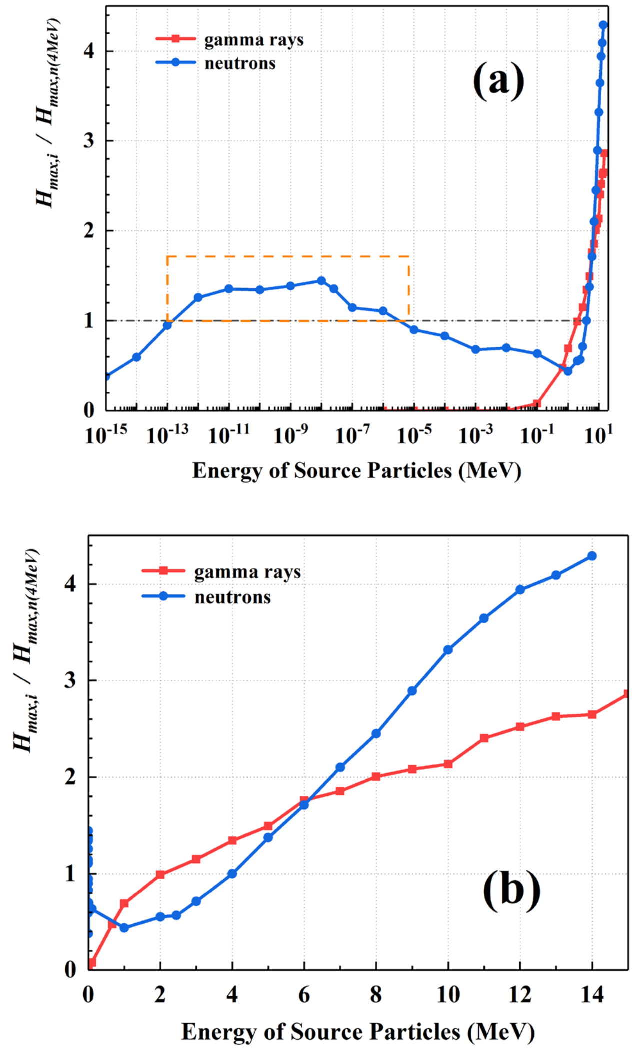

Fig. 3 (Color online) Ratio of the maximum height of the output signals produced by neutrons and gamma rays of different energies ($H_{\max,i}$) in the Sci-Fi detector to the corresponding maximum height of the 4-MeV neutron signals ($H_{\max,n(4\,\mathrm{MeV})}$). The two subgraphs are presented in the (**a**) logarithmic and (**b**) linear coordinates

accounted for the effects of both neutrons and gamma rays, whereas the simulation of ^{137}Cs was substituted with a 0.662-MeV gamma-ray source. Based on the activity, yield, and measurement time of each radioactive source, the counts obtained from the experiments and simulations were converted based on the experimental measurement results of ^{252}Cf, to presented in the same figure.

4.1 $H_{\max}$ ratio of different particle sources

To reduce accidental errors, a new horizontal baseline similar to that used in [26] was selected when counting the maximum heights of the output pulse signals caused by different particle sources. This implied that only data points with a corresponding count of 10 or more were considered. In addition, to reduce subjective errors further, the pulse height spectra were smoothed based on the CERN ROOT framework [37].

The Sci-Fi detector exhibited a significant difference in the $H_{\max}$ ratio of the neutron and gamma-ray sources, as shown in Fig. 3. Note that the $H_{\max,i}/H_{\max,n(4\,\mathrm{MeV})}$ is used to represent the $H_{\max}$ ratio, and i represents the type and energy of the particles corresponding to the color of the curve and coordinates on the horizontal axis, respectively. Cold neutrons of extremely low energy ($<10^{-9}$ MeV) are rare, and their corresponding data points serve only as a reference. The response curve of the maximum pulse height of gamma rays displays good linearity, whereas the neutron response curve exhibits nonlinear characteristics in both the low-energy and high-energy regions.

The measurement effect of the Sci-Fi detector on neutrons above 10 MeV may be affected by the size of the Sci-Fi. Because the energy of the recoil proton is positively correlated with the energy of the incident neutron, the higher the energy of the recoil proton, the less likely it is to deposit all energy in only the 1 mm diameter fiber. Consequently, the response curve of the detector to neutrons in this energy range exhibits gradual nonlinearity.

The abnormal $H_{\max}$ ratio curve of the neutrons in the low-energy region can be attributed to the impact of numerous secondary particles generated by incident neutrons in the magnetic shielding tube, such as high-energy gamma rays, and, to a lesser extent, to the effect of secondary particles generated in the detector shell and substrate. The capture reaction cross sections of the permalloy and pure aluminum increased with decreasing neutron energy, resulting in a significant increase in the maximum signal height in the low-energy region. The black horizontal line in Fig. 3a represents the $H_{\max,\mathrm{n}(4\,\mathrm{MeV})}$. It can be observed that when the energy of the neutron source is within the range corresponding to the yellow box, the $H_{\max,i}$ of the incident neutrons can reach a level similar to that of fast neutrons. Considering the high thermal neutron flux around EAST during operation, this abnormality in the $H_{\max}$ ratio curve can adversely affect the D–T neutron resolution of the Sci-Fi detector, which is mainly reflected in the following aspects:

1. The pulse signals generated by neutrons above 4 MeV in the detector may be confused with signals from low-energy neutrons, which can cause large errors in the calibration according to the NAS
2. Dense thermal neutron signals may saturate the detector, causing stacked signals and resulting in distortion of the measured energy spectra

The gamma rays around EAST were mostly concentrated in the low-energy region, and their pulse signals did not exceed $H_{\max,n(4\,\mathrm{MeV})}$. However, there are still a small number of gamma rays above 2 MeV, which can interfere with D–T neutron discrimination, as shown in Fig. 3b. Although this situation occurs with a low probability (e.g., less than 1% of the 2-MeV gamma rays produce signals higher than $H_{\max,\mathrm{n}(4\,\mathrm{MeV})}$), it is necessary to shield these high-energy gamma rays. Currently, a commonly used method is employing a large external shield made of heavy metals such as lead (Pb) or tungsten (W), which was not considered in this study because of its excessively large volume and weight. In contrast, a compact shield for low-energy gamma rays and neutrons, particularly thermal neutrons, which is small and can be combined with the magnetic shielding tube, was designed in this study.

4.2 Design of the thermal neutron shield

Thermal neutrons should be shielded outside the magnetic shielding tube to avoid interactions with the permalloy. The commonly used absorbing materials are boron (B) and cadmium (Cd), which have high reaction cross sections for thermal neutrons. Cd is preferred because of its higher density and volume limitation of the detector system. Cd with a thickness of 1 mm has a good absorption effect on thermal neutrons and was therefore used directly in this study. For the numerous gamma rays generated by the neutron capture reaction and subsequent β rays, they should also be prevented from entering the head of the Sci-Fi detector. Pb and W are suitable shielding materials and both have high densities. Here Pb was used as a secondary shield (inner shield) located in the magnetic shielding tube to reduce the overall weight. Figure 4 illustrates the $H_{\max}$ ratio curve of the complete detector models when thermal neutron shields consisting of a 1-mm outer Cd layer and an inner Pb layer of four different thicknesses were used. Note that the red dotted line represents the $H_{\max,\mathrm{n}(4\,\mathrm{MeV})}$, and "shield" in the legend of Fig. 4, and the subsequent figures refer to the thermal neutron shield only.

As shown in Fig. 4, a thermal neutron shield with an inner Pb layer thickness of 1 mm can effectively reduce the maximum height of the pulse signals generated by thermal neutrons of most energies to an ideal level. However, for some neutrons of slightly higher energy (~ 10^{-5} MeV), this design

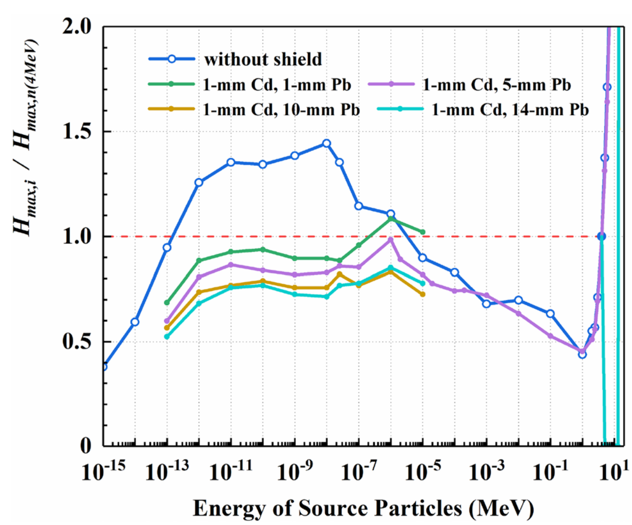

Fig. 4 (Color online) Effect of thermal neutron shield composed of 1-mm outer Cd layer and inner Pb layer of several thicknesses on $H_{\max}$ ratio of low-energy neutrons

can even lead to higher-amplitude output signals, which may be related to the absorption effect of the Cd layer outside the magnetic shielding tube on the neutrons. As the neutron energy increases, the capture cross section of Cd in the low-energy range decreases, resulting in an insufficient capture capacity for neutrons above and near 10^{-6} MeV; therefore, residual neutrons may produce extra secondary particles in the inner Pb layer. At the same time, the 1-mm Pb layer could not sufficiently shield the gamma rays generated by the neutron capture reaction in this case. The combined effects of these factors resulted in the peak of $H_{\max}$ ratio being observed at 10^{-6} MeV.

Increasing the thickness of the Cd layer has little effect on this issue, whereas thickening the inner Pb layer could address this problem. When the inner Pb layer thickness was increased to 5 mm, the $H_{\max,i}$ of the neutrons in the low-energy range was suppressed below $H_{\max,\mathrm{n}(4\,\mathrm{MeV})}$, and the peak height at 10^{-6} MeV was reduced to an acceptable level. A thicker inner Pb layer results in a further reduction in the peak height, thus enhancing the resistance of the detector to low-energy neutron interference. However, the also enhanced shielding effect on incident fast neutrons is detrimental to D–T neutron measurement and increases the volume and weight of the shield. Therefore, considering the space constraints around EAST, a thermal neutron shield design scheme with an outer 1-mm Cd layer and inner 5-mm Pb layer was selected. If the thermal neutron flux in the environment is excessively high, the shield thickness may need to be appropriately increased.

Simulation studies evaluated the impact of the thermal neutron shield on the pulse height spectra of the Sci-Fi detector when measuring fast neutrons and gamma rays; the resulting statistics of $H_{\max}$ ratio are shown in Fig. 5. Note that the data points corresponding to extremely low-energy ($< 10^{-9}$ MeV) neutrons were used for reference only. For gamma rays with energies greater than 2 MeV, the shield can reduce the $H_{\max}$ ratio by 8.95% on average. In addition, the minimum energy corresponding to the $H_{\max}$ ratio curve of gamma rays is cut off an order of magnitude earlier (Fig. 5a) because lower-energy gamma rays are easily absorbed by the Pb layer and cannot enter the sensitive volume of the detector. Consequently, the Sci-Fi detector has a better ability to suppress gamma-ray signals when the thermal neutron shield is used; however, this effect is mainly reflected in avoiding count saturation and signal accumulation. Gamma rays above 2 MeV can still produce high-amplitude signals; therefore, shielding against high-energy gamma rays in the environment may be the key to further improving the D–T neutron discrimination capability of the Sci-Fi detector in actual use. When the incident particle is a neutron, the thermal neutron shield also causes a decrease in the $H_{\max}$ ratio. The average decrease was 4.56% for fast neutrons above 4 MeV and 31.16% for low-energy neutrons below 10^{-5} MeV. The shield unavoidably affects D–T neutron detection. As the thermal neutron flux is generally much higher than the fast neutrons in the neutron energy spectra during EAST operation, using a suitable thickness of the thermal neutron shield is reasonable.

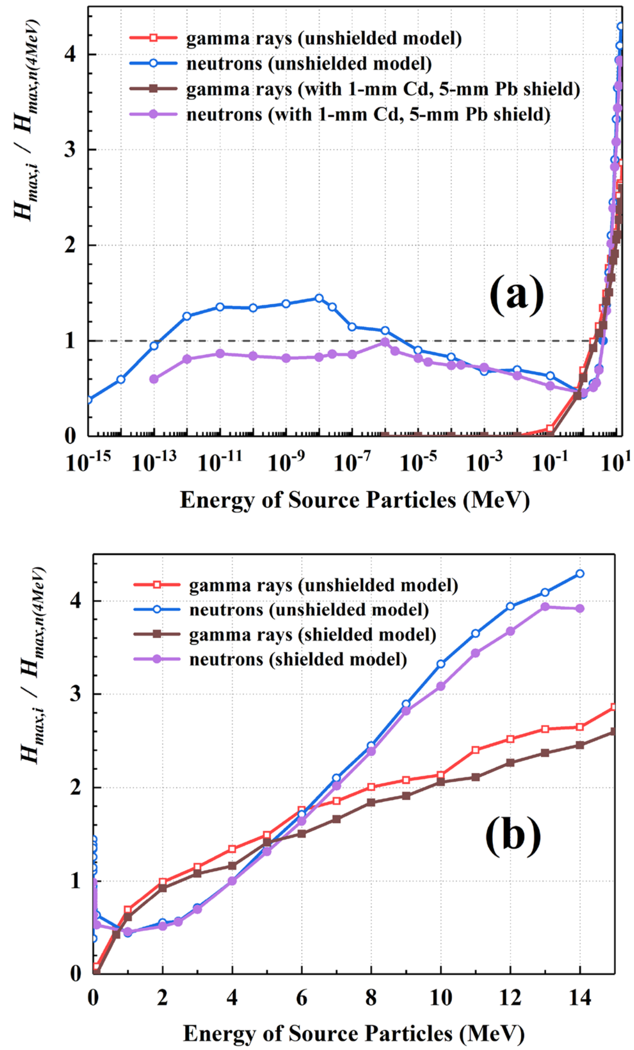

Fig. 5 (Color online) Effect of a thermal neutron shield composed of a 1-mm outer Cd layer and a 5-mm inner Pb layer on the $H_{\max}$ ratio of incident neutrons and gamma rays with different energies. The two subgraphs are presented in the (**a**) logarithmic and (**b**) linear coordinates

In addition, the number of pulse signals higher than $H_{\max,\mathrm{n}(4\,\mathrm{MeV})}$ generated by incident neutrons and gamma rays of different energies was counted. The results reveal that using the thermal neutron shield reduces the number of eligible signals for gamma rays above 2 MeV by 29.71% and for low-energy neutrons below 10^{-5} MeV by 74.07%; however, for fast neutrons above 4 MeV, the loss ratio of effective signals is only 8.59%. This indicates that the effect of the thermal neutron shield is acceptable from this perspective.

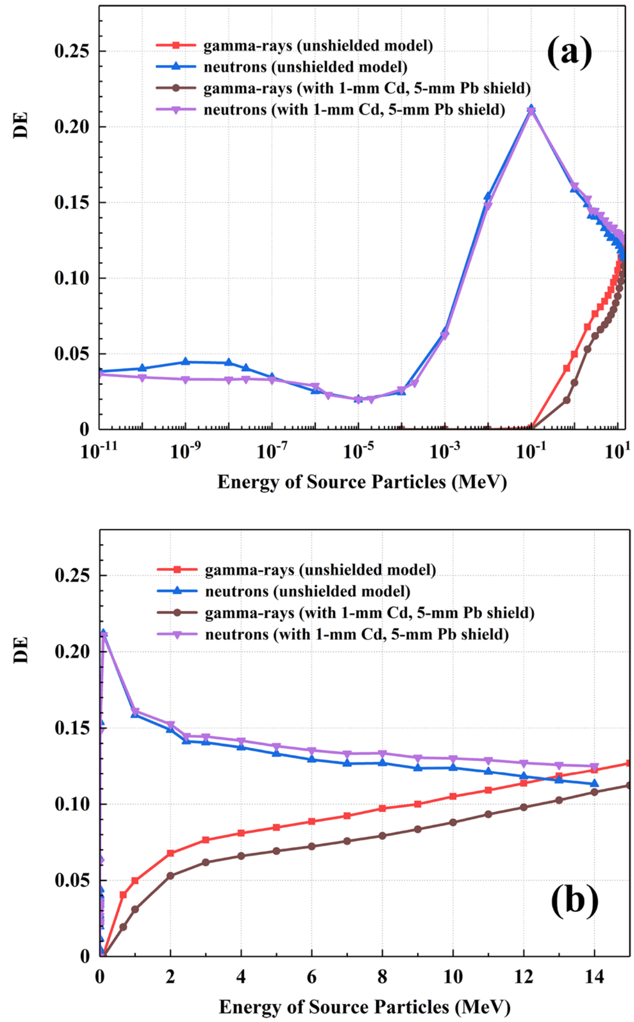

Fig. 6 (Color online) DEs of the Sci-Fi detector with and without a thermal neutron shield. The two subgraphs are presented in the (**a**) logarithmic and (**b**) linear coordinates

4.3 Energy response of the Sci-Fi detector

Figure 6 illustrates the DEs of the Sci-Fi detector model for neutrons and gamma rays with different energies, along with the response curves of the new complete model that includes the thermal neutron shield. The detector exhibited a relatively flat response curve to fast neutrons compared to gamma rays and low-energy neutrons. Still using the DE for 4-MeV neutrons as a baseline, when the energy of neutron source rises to 14 MeV, the DE of the complete detector model using the thermal neutron shield is reduced by 11.80%, whereas the DE of the case not using the shield is reduced by 17.60%. This reduction may be related to the neutron reaction cross sections of elements such as hydrogen (H). Note that the flat response curve of the Sci-Fi detector to fast neutrons is advantageous for D–T fusion neutron measurement on EAST because the neutrons emitted from the plasma may be scattered multiple times and lose energy in the surrounding environment, and these processes cannot be predicted. At present, the detector uses the same calibration factor for the measurement of neutrons above 4 MeV; therefore, it is crucial to ensure that the sensitivity of the detector to these neutrons is approximately equal. In addition, as more accurate measurements may be required in the future, the response curves obtained in this study can be used as a reference to set independent calibration factors for each energy range.

Figure 6a shows that the Sci-Fi detector had high DEs for neutrons in the energy range of 10^{-3}–1 MeV. However, as the signal acquisition system on EAST typically employs a low threshold to prevent the acquisition of useless but numerous low-amplitude signals, we computed the DEs additionally when a low threshold was set and present the results in Fig. 7. In this case, the DEs of the entire detector system for the 10^{-3}–1-MeV neutrons were significantly

Fig. 7 (Color online) DEs of the Sci-Fi detector system for neutrons of different energies when a low signal acquisition threshold was applied

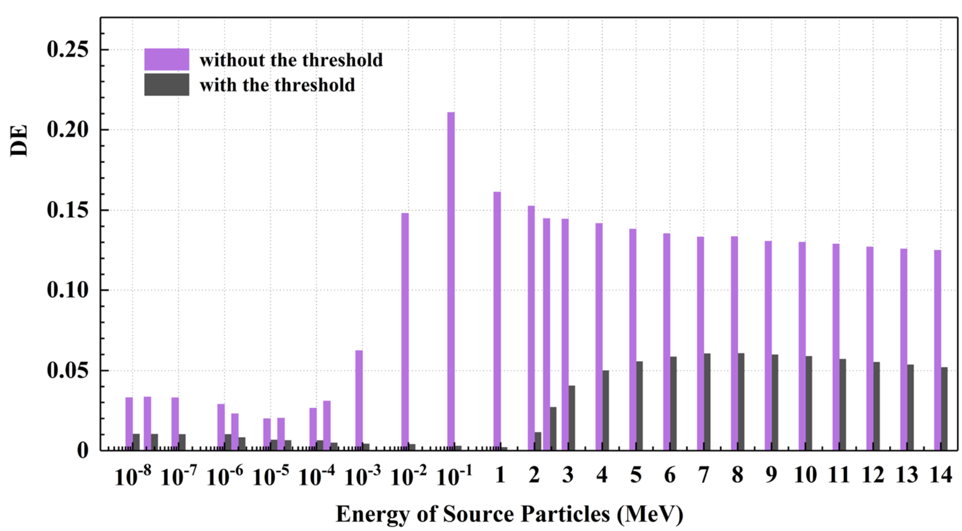

suppressed. Therefore, the signal acquisition threshold is an important factor affecting the detection performance of the Sci-Fi detector in practice.

In addition, the complete detector models with and without the thermal neutron shield exhibited lower DEs for neutrons and gamma rays than expected. This is because the magnetic shielding tube is regarded as a necessary component of the Sci-Fi detector system. Thus, the statistical $N_{\mathrm{in,front}}$ is based on the front surface of the magnetic shielding tube. In fact, the diameter of the detector head is only half that of the magnetic shielding tube; therefore, the number of incident source particles entering the detector head is much smaller than that of $N_{\mathrm{in,front}}$, resulting in lower DEs. Scattering of incident particles by the magnetic shielding tube may also lead to lower DEs at the same time. To avoid these effects, the IDE was used as another evaluation criterion for the detection effect, as shown in Fig. 8. In addition, the particles entering the detector head include not only the source particles but also some secondary particles generated in other components, such as the magnetic shielding tube and thermal neutron shield.

The total number of these events is expressed as $N_{\mathrm{in(allP),eff}}$, which includes the $N_{\mathrm{in,eff}}$ that has been defined in this paper. The latter can also be written as $N_{\mathrm{in(srcP),eff}}$ to make a distinction. When the neutron source was used, the $N_{\mathrm{in(srcP),eff}}$ was converted to $N_{\mathrm{in(srcN),eff}}$; meanwhile, the events in which only secondary particles entered the detector head were contained in $N_{\mathrm{in(allP),eff}}$. It is important to emphasize that the output signals produced by these secondary particles alone cannot reflect the true states of the source neutrons and are considered to interfere with neutron measurement. In contrast, only when the incident particles entering the detector head contained neutrons were events required for neutron detection. The proportion of $N_{\mathrm{in(srcN),eff}}$ in $N_{\mathrm{in(allP),eff}}$ is shown in Fig. 8 to characterize the influence of secondary particles generated by source neutrons. The low proportion indicates that most of the output signals may be caused by secondary particles generated in the outer components of the complete detector model, such as the thermal neutron shield and magnetic shielding tube, rather than by source neutrons.

The IDE can better reflect the performance of the detector itself than the DE, without being affected by the particle source or outside environment. As shown in Fig. 8, the Sci-Fi detector exhibits high sensitivity to the source particles that enter the detector head. The IDE for fast neutrons is as high as 40%, whereas for gamma rays of not quite high energy (< 8 MeV) around the EAST device, the IDE is typically approximately 20%. Note that the IDE curve for low-energy gamma rays is truncated at less than 0.1 MeV owing to the inability of such rays to penetrate the magnetic shielding tube; however, with the inclusion of the thermal neutron shield and owing to the presence of the inner Pb layer, the cutoff occurs an order of magnitude earlier.

In addition, Fig. 8a shows that the IDE curve of the neutrons exhibits an upward trend when the energy is less than 10^{-5} MeV. To clarify this, the statistics on $N_{\mathrm{in(srcN),eff}}/N_{\mathrm{in(allP),eff}}$ indicate that, when the energy of the neutron source is excessively low (< 10^{-5} MeV), the signals output by the Sci-Fi detector may be partly or fully produced by secondary particles rather than source neutrons. This phenomenon is more evident when a thermal neutron

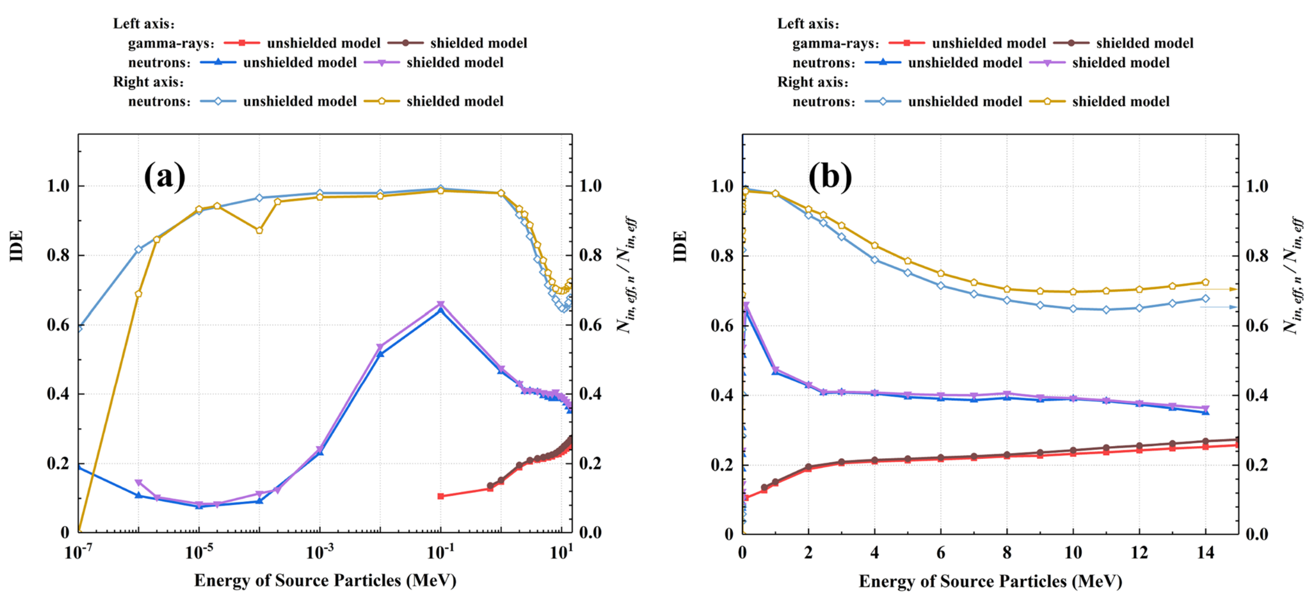

Fig. 8 (Color online) Left axis: IDEs of the Sci-Fi detector for incident neutrons and gamma rays of different energies. Right axis: proportion of the $N_{\mathrm{in(srcN),eff}}$ to $N_{\mathrm{in(allP),eff}}$. The two subgraphs are presented in the (**a**) logarithmic and (**b**) linear coordinates

shield is employed. The pit on the IDE curve when the source neutron energy is 10^{-4} MeV may be due to the resonance absorption of neutrons in the Cd layer. Additionally, the $N_{\mathrm{in(srcN),eff}}/N_{\mathrm{in(allP),eff}}$ values in Fig. 8b are only approximately 70% in the fast neutron region, which implies that some of the fast neutron signals detected by the Sci-Fi detector are also caused by secondary particles. These signals are typically low in amplitude and may, therefore, be the reason for the reduced DEs of fast neutrons when the signal acquisition threshold is set, as shown in Fig. 7. Meanwhile, the value of $N_{\mathrm{in(srcN),eff}}/N_{\mathrm{in(allP),eff}}$ was slightly higher when the thermal neutron shield was used. These two factors may have contributed to the phenomenon:

1. The enhanced scattering of incident neutrons by the thermal neutron shield led to an increase in $N_{\mathrm{in(srcN),eff}}$;
2. The absorption of secondary particles by the inner Pb layer of the thermal neutron shield reduces the number of events in which only secondary particles enter the detector head in $N_{\mathrm{in(allP),eff}}$

5 Conclusion

The new Sci-Fi detector inside the magnetic shielding tube was designed and assembled, and will be used in the next round of fusion experiments on EAST to provide D–T neutron yield with time resolution. The selection of appropriate amplitude thresholds for the output signals is the basis for a Sci-Fi detector that realizes D–T neutron discrimination. To coordinate and calibrate with the existing NAS, the maximum height of the interfering particle signals should be lower than that of the signals corresponding to 4-MeV neutrons. In this study, the pulse height spectra of the signals produced when neutrons and gamma rays of multiple energies entered the complete detector models were obtained using the Geant4 simulation. Low-energy neutrons below 10^{-5} MeV and gamma rays above 2 MeV were the primary sources of interference owing to their high-amplitude output signals. Further simulations with and without the magnetic shielding tube revealed that the secondary particles generated by low-energy neutrons in the tube were a significant factor leading to this phenomenon. To address this issue, a compact thermal neutron shield containing a 1 mm Cd layer outside the magnetic shielding tube and a 5 mm inner Pb layer was specifically designed. It can effectively suppress the output signals caused by thermal neutrons to the target level. Moreover, its adverse effects on the measurement of neutrons above 4 MeV and shielding effect on gamma rays above 2 MeV were evaluated as relatively acceptable. In addition, energy response studies with and without the thermal neutron shield in the Sci-Fi detector model revealed that, in both cases, the detector had relatively flat sensitivity curves in the fast neutron region, and the IDEs were approximately 40%. For gamma rays of not quite high energy (< 8 MeV), the IDEs of the detector were only about 20%, indicating that the difference of IDEs between neutrons and gamma rays was also a contributing factor in achieving good *n*/*γ* resolution of the Sci-Fi detector. The low-energy gamma rays were blocked by the inner Pb layer of the thermal neutron shield, resulting in an earlier cutoff of the detector's response curve to gamma rays in the low-energy region, which was beneficial for avoiding count saturation and signal accumulation. The study also found that shielding high-energy gamma rays in the environment may be the key to further improving the D–T neutron discrimination capability of the Sci-Fi detector in actual use.

Author contribution All authors contributed to the study conception and design. Material preparation, data collection, and analysis were performed by Wei-Kun Chen, Li-Qun Hu, Guo-Qiang Zhong, Rui-Jie Zhou, Bing Hong, Qiang Li, and Li Yang. The first draft of the manuscript was written by Wei-Kun Chen, and all authors commented on previous versions of the manuscript. All authors read and approved the final manuscript.

Data availability The data that support the findings of this study are openly available in Science Data Bank at https://doi.org/10.57760/sciencedb.j00186.00053 and https://cstr.cn/31253.11.sciencedb.j00186.00053.

Declarations

Conflict of interest The authors declare that they have no competing interests.

References

1. K. Ogawa, M. Isobe, S. Sangaroon et al., Time-resolved secondary triton burnup 14 MeV neutron measurement by a new scintillating fiber detector in middle total neutron emission ranges in deuterium large helical device plasma experiments. AAPPS Bull. **31**, 20 (2021). https://doi.org/10.1007/s43673-021-00023-2
2. J.R. Smith, R.K. Fisher, J.S. Leffler et al., Time-resolved 14-MeV neutron detector for triton confinement studies. Rev. Sci. Instrum. **57**, 1780–1782 (1986). https://doi.org/10.1063/1.1139180
3. H.H. Duong, W.W. Heidbrink, Confinement of fusion produced MeV ions in the DIII-D tokamak. Nucl. Fusion **33**, 211–224 (1993). https://doi.org/10.1088/0029-5515/33/2/i03
4. P. Batistoni, M. Martone, M. Pillon et al., Measurements of triton burnup in low Q discharges in the FT tokamak. Nucl. Fusion **27**, 1040–1043 (1987). https://doi.org/10.1088/0029-5515/27/6/017
5. P. Batistoni, E. Bittoni, M. Haegi, Triton confinement as inferred from fusion from fusion produced neutron measurements in the FT tokamak. Nucl. Fusion **29**, 673–679 (1989). https://doi.org/10.1088/0029-5515/29/4/011
6. G.A. Wurden, R.E. Chrien, C.W. Barnes et al., Scintillating-fiber 14 MeV neutron detector on TFTR during DT operation. Rev. Sci. Instrum. **66**, 901–903 (1995). https://doi.org/10.1063/1.1146200
7. J.S. McCauley, J.D. Strachan, Measurement of DT neutron emission from TFTR with helium-4 proportional recoil counters. Rev.

Sci. Instrum. **63**, 4536–4538 (1992). https://doi.org/10.1063/1.1143712
8. C.W. Barnes, H.S. Bosch, H.W. Hendel et al., Triton burnup measurements and calculations on TFTR. Nucl. Fusion **38**, 597–618 (1998). https://doi.org/10.1088/0029-5515/38/4/310
9. J. Kallne, P. Batistoni, G. Gorini et al., Triton burnup measurements in JET using a neutron-activation techniques. Nucl. Fusion **28**, 1291–1297 (1988). https://doi.org/10.1088/0029-5515/28/7/012
10. G. Nemtsev, V. Amosov, S. Meshchaninov et al., Study of the triton-burnup process in different JET scenarios using neutron monitor based on CVD diamond. Rev. Sci. Instrum. **87**, 11D835 (2016). https://doi.org/10.1063/1.4962190
11. F.B. Marcus, J.M. Adams, B. Balet et al., Neutron emission profile measurements during the 1st tritium experiments at JET. Nucl. Fusion **33**, 1325–1344 (1993). https://doi.org/10.1088/0029-5515/33/9/i08
12. W. Ullrich, H.S. Bosch, F. Hoenen, Application of a Si-diode detector for fusion product measurements in ASDEX upgrade. Rev. Sci. Instrum. **68**, 4434–4438 (1997). https://doi.org/10.1063/1.1148410
13. J. Jo, M.S. Cheon, K.-J. Chung et al., Sample design and gamma-ray counting strategy of neutron activation system for triton burnup measurements in KSTAR. Fusion Eng. Des. **109–111**, 545–548 (2016). https://doi.org/10.1016/j.fusengdes.2016.02.058
14. J. Jo, M. Cheon, J.Y. Kim et al., Triton burnup measurements in KSTAR using a neutron activation system. Rev. Sci. Instrum. **87**, 11D828 (2016). https://doi.org/10.1063/1.4961273
15. J. Jo, M. Cheon, J. Kim et al., Initial operation results of NE213 scintillation detector for time-resolved measurements on triton burnup in KSTAR. Rev. Sci. Instrum. **89**, 10I118 (2018). https://doi.org/10.1063/1.5039308
16. N. Pu, T. Nishitani, K. Ogawa et al., Scintillating fiber detectors for time evolution measurement of the triton burnup on the large helical device. Rev. Sci. Instrum. **89**, 10I105 (2018). https://doi.org/10.1063/1.5035290
17. N. Pu, T. Nishitani, M. Isobe et al., Evaluation of scintillating-fiber detector response for 14 MeV neutron measurement. J. Instrum. **14**, P10015 (2019). https://doi.org/10.1088/1748-0221/14/10/p10015
18. K. Ogawa, M. Isobe, H. Nuga et al., A study of beam ion and deuterium–deuterium fusion-born triton transports due to energetic particle-driven magnetohydrodynamic instability in the large helical device deuterium plasmas. Nucl. Fusion **61**, 096035 (2021). https://doi.org/10.1088/1741-4326/ac0d8a
19. K. Ogawa, M. Isobe, T. Nishitani et al., Time-resolved triton burnup measurement using the scintillating fiber detector in the large Helical device. Nucl. Fusion **58**, 034002 (2018). https://doi.org/10.1088/1741-4326/aaa585
20. T. Nishitani, M. Isobe, G.A. Wurden et al., Triton burnup measurements using scintillating fiber detectors on JT-60U. Fusion Eng. Des. **34–35**, 563–566 (1997). https://doi.org/10.1016/s0920-3796(96)00621-7
21. T. Nishitani, M. Hoek, H. Harano et al., Triton burn-up study in JT-60U. Plasma Phys. Control. Fusion **38**, 355–364 (1996). https://doi.org/10.1088/0741-3335/38/3/010
22. M. Hoek, T. Nishitani, M. Carlsson et al., Triton burnup measurements by neutron activation at JT-60U. Nucl. Instrum. Methods Phys. Res Sect. A **368**, 804–814 (1996). https://doi.org/10.1016/0168-9002(95)00667-2
23. S. Wu, An overview of the EAST project. Fusion Eng. Des. **82**, 463–471 (2007). https://doi.org/10.1016/j.fusengdes.2007.03.012
24. K. Li, L. Hu, G. Zhong et al., Development of neutron activation system on EAST. Rev. Sci. Instrum. **91**, 013503 (2020). https://doi.org/10.1063/1.5126746
25. B. Hong, G.Q. Zhong, L.Q. Hu et al., Diagnostic of fusion neutrons on EAST tokamak using 4H-SiC detector. IEEE Trans. Nucl. Sci. **69**, 639–644 (2022). https://doi.org/10.1109/tns.2022.3146180
26. W.-K. Chen, L.-Q. Hu, G.-Q. Zhong et al., Optimization study and design of scintillating fiber detector for D-T neutron measurements on EAST with Geant4. Nucl. Sci. Tech. **33**, 139 (2022). https://doi.org/10.1007/s41365-022-01123-w
27. Atlas of Neutron Capture Cross Sections. https://www-nds.iaea.org/ngatlas2/
28. N. Metropolis, S. Ulam, The monte carlo method. J. Am. Stat. Assoc. **44**, 335–341 (1949). https://doi.org/10.1080/01621459.1949.10483310
29. Kuraray scintillation fiber. http://kuraraypsf.jp/psf/index.html
30. S. Agostinelli, J. Allison, K. Amako et al., Geant4—a simulation toolkit. Nucl. Instrum. Methods Phys. Res Sect. A **506**, 250–303 (2003). https://doi.org/10.1016/s0168-9002(03)01368-8
31. Z. Cheng, Y. Yu, G. Li et al., Measurement of attenuation length and light yield of plastic scintillating fiber with silicon photomultiplier. At. Energy Sci. Technol. **54**, 340–347 (2020). https://doi.org/10.7538/yzk.2019.youxian.0221. (**in Chinese**)
32. R.J. Zhou, G.Q. Zhong, L.Q. Hu et al., Development of gamma ray spectrometer with high energy and time resolutions on EAST tokamak. Rev. Sci. Instrum. **90**, 123510 (2019). https://doi.org/10.1063/1.5120843
33. M. Xu, G. Zhong, B. Hao et al., Excitation of RSAEs during sawteeth-like oscillation in EAST. Chin. Phys. Lett. **38**, 085201 (2021). https://doi.org/10.1088/0256-307x/38/8/085201
34. Z. Xu, Z.-W. Wu, L. Zhang et al., Tungsten control in type-I ELMy H-mode plasmas on EAST. Nucl. Sci. Tech. **32**, 95 (2021). https://doi.org/10.1007/s41365-021-00929-4
35. J.-F. Wang, Y.-Y. Li, B. Wu et al., Numerical and experimental evaluation of shine-through loss and beam heating due to neutral beam injection on EAST. Chin. Phys. Lett. **38**, 055203 (2021). https://doi.org/10.1088/0256-307x/38/5/055203
36. X. Zhang, C. Zhou, X. Zou et al., Edge localized modes suppression via edge E × B velocity shear induced by RF sheath of ion cyclotron resonance heating in EAST. Sci. China Phys. Mech. Astron. **65**, 235211 (2022). https://doi.org/10.1007/s11433-021-1817-8
37. I. Antcheva, M. Ballintijn, B. Bellenot et al., ROOT—a C++ framework for petabyte data storage, statistical analysis and visualization. Comput. Phys. Commun. **180**, 2499–2512 (2009). https://doi.org/10.1016/j.cpc.2009.08.005